

Radio-Frequency Electric Field Sensing Based on a Single Solid-State Spin

Zhi Cheng,^{1,2,§} Xiangyu Ye,^{1,2,§} Jiandong Wu,^{3,4,§} Pei Yu,^{1,2} Cheng-Jie Wang,^{1,2} Mengqi Wang,^{1,2}
Chang-Kui Duan,^{1,2} Ya Wang,^{1,2,5} Fazhan Shi,^{1,2,5} Changlin Tian,^{3,6} Hongwei Chen,^{3,*}
Pengfei Wang,^{1,2,5,†} and Jiangfeng Du,^{1,2,5,‡}

¹CAS Key Laboratory of Microscale Magnetic Resonance and School of Physical Sciences, University of Science and Technology of China, Hefei 230026, China


²CAS Center for Excellence in Quantum Information and Quantum Physics, University of Science and Technology of China, Hefei 230026, China

³High Magnetic Field Laboratory, Hefei Institutes of Physical Science, Chinese Academy of Sciences, Hefei 230031, China

⁴Institutes of Physical Science and Information Technology, Anhui University, Hefei 230601, China

⁵Hefei National Laboratory, University of Science and Technology of China, Hefei 230088, China

⁶High Magnetic Field Laboratory, Hefei Institutes of Physical Science, Chinese Academy of Sciences, Hefei 230031, China

 (Received 17 June 2022; revised 7 December 2022; accepted 7 December 2022; published 20 January 2023; corrected 8 February 2023)

Nanoscale amplitude and phase sensing of a rf electromagnetic field can benefit broad frontiers in science and technology. The imaging applications in these research areas demand a nanoscale sensor able to detect rf electric fields over a wide frequency range under ambient conditions, which remains a challenge. Here, we present a rf electrometry based on the forbidden magnetic dipole transition of a single shallow nitrogen-vacancy center in diamond and experimentally demonstrate the detection of rf electric fields at frequencies ranging from 13.85 MHz to 2.02 GHz. A sensitivity of $265 \text{ V cm}^{-1} \text{ Hz}^{-1/2}$ for amplitude measurement and a standard deviation of 0.2° for phase measurement are achieved. The potential applications of nanoscale sensing and imaging of electromagnetic field are discussed.

DOI: [10.1103/PhysRevApplied.19.014057](https://doi.org/10.1103/PhysRevApplied.19.014057)

I. INTRODUCTION

The sensing of rf electric fields plays a significant role in a broad range of fundamental science and advanced information technology. Particularly in the nanoscale, it can enable a variety of studies, such as nanoscale electromagnetism [1], the axion [2], ferroelectrics, and the nanochip. For example, mapping the relationship between nanopolar structures and the high-frequency dynamic response remains a central problem in tunable ferroelectrics devices [3,4]. Moreover, the electric and magnetic fields have no straightforward relationship in the near field of rf radiation, see Refs. [5,6] and the Appendix. It means that the rf electric field cannot be generally calculated by the measurement of the rf magnetic field in the near-field region, which makes it significant to develop a rf electric field sensor at the fine-space scale (see the Appendix for detailed discussion).

In recent decades, rf electrometry has been demonstrated by the open-ended coaxial tip [6,7] and lab-on-fiber technology [8,9] as well as several well-defined quantum systems such as Rydberg atoms [10–12] and trapped ions [13]. Although incredible sensitivities have been achieved in these systems, their limited spatial resolution prohibits them from nanoscale sensing applications. Our approach adopts an atomic point defect in diamond termed the nitrogen-vacancy (N-V) center [14], which has been developed as a nanoscale quantum sensor for multiple physical quantities [15] in recent years. The spin-triplet ground states of N-V center has been demonstrated to be sensitive to the magnetic field ranging from direct current to microwave (MW) band [16–18]. Meanwhile, the mixing of the orbital and spin components of electronic states allows the presence of the Stark effect in the ground states. Thus the ground spin triplet of the N-V center is also sensitive to electric fields. The detection from static to up to sub-MHz electric fields based on N-V centers has been reported in previous works [19–22]. However, detection of rf electric fields of high frequency ($> 100 \text{ MHz}$) has remained challenging because the electronic spin must be flipped at the same frequency of the rf fields, which is technically unachievable at present.

*hwchen@hmfll.ac.cn

†wpf@ustc.edu.cn

‡djf@ustc.edu.cn

§These authors contributed equally to this work.

In this paper, we propose and experimentally demonstrate a simple scheme for amplitude and phase sensing of rf electric fields using a shallow N-V center. The scheme adopts the electrically driven transition of the electron spin, which enables the rf electric field sensing and the electric manipulation of quantum states. Next, we show that the scheme allows us to co-measure the electric and magnetic components of a rf electromagnetic field from the same capacitive device. Furthermore, we estimate the influence of the surface effect and the dielectric function by measuring the frequency response from 13.85 MHz to 2.02 GHz, which is approximately constant and suggests a flat detection window for rf fields. Finally, we discuss the potential imaging applications based on this scheme.

II. ELECTRICALLY DRIVEN TRANSITION

The N-V center in diamond consists of a substitutional nitrogen atom and an adjacent carbon vacancy. The ground state triplet of the N-V center can be initialized and readout via optical excitation, which enables the implementation of the optically detected magnetic resonance (ODMR) technique [see Fig. 1(a)]. In this work, a diamond layer grown by microwave-assisted chemical vapor deposition with 99.999% ^{12}C enriched methane is used as the carrier of the N-V center. The N-V centers are generated by 2.5 keV $^{15}\text{N}^+$ ion implantation followed by annealing in high vacuum [23]. The implanted N-V centers are distinguished from the natural ones according to the ^{15}N hyperfine-coupled nuclear spin. A gold stripline and a pair of gold electrodes fabricated on the diamond surface are used to deliver MW magnetic fields for quantum state manipulation and rf electric field to be detected. An N-V center between the electrodes and near the stripline is located and applied for all the following experiments.

The Hamiltonian of the N-V center under the static magnetic field, including the electron spin term, the nuclear spin term, and the hyperfine coupling term is written as

$$H_{\text{GS}} = D_{\text{GS}}S_z^2 + B_z(\gamma_e S_z + \gamma_N I_z) + \mathbf{S} \cdot \mathbf{A} \cdot \mathbf{I}, \quad (1)$$

where D_{GS} is the zero-field splitting, γ_e and γ_N are the gyromagnetic ratios of electron spin and the ^{15}N nuclear spin, respectively. $\mathbf{S} = (S_x, S_y, S_z)$ are the electron spin-1 operators, $\mathbf{I} = (I_x, I_y, I_z)$ are the nuclear spin-1/2 operators, and \mathbf{A} is the hyperfine coupling tensor for the electron spin and the nuclear spin. In the following, we denote the A_{zz} component as A .

We first consider the subspace of the electron spin. In the presence of the rf electric field that is tuned to be on resonance, the corresponding Hamiltonian is

$$H_{\text{rf}}^E = d_{\perp} \left[E_x(t) (S_x^2 - S_y^2) - E_y(t) (S_x S_y + S_y S_x) \right], \quad (2)$$

where $d_{\perp} = (17 \pm 3) \text{ Hz cm V}^{-1}$ is the N-V centers' nonaxial electric dipole moment [19]. $E_x(t) =$

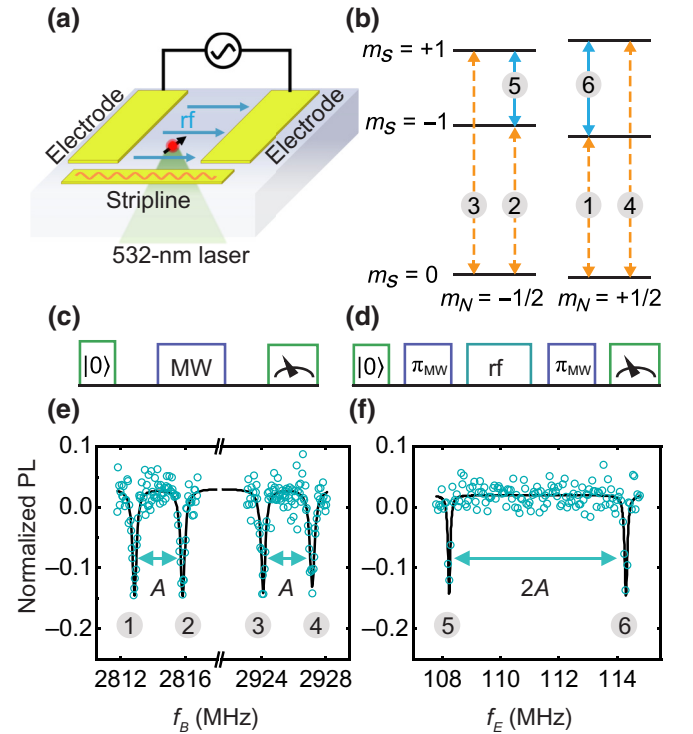


FIG. 1. (a) Schematic view of the experimental setup. (b) The energy levels of the N-V center. The magnetically driven transitions labeled 1,2,3,4 of which $\Delta m_s = \pm 1$ and the forbidden transitions labeled 5,6 of which $\Delta m_s = \pm 2$ are shown by the orange dashed line and the blue solid line, respectively. (c),(d) Sequences for optically detected magnetic resonance spectrum and the optically detected electric resonance spectrum. (e),(f) Optically detected magnetic resonance spectrum and the optically detected electric resonance spectrum of the N-V center, where f_B and f_E are the frequencies for the magnetic and electric fields, respectively. The labeled resonance peaks correspond to the same transitions as in (b). The results of the Lorentz fit show splittings of 3 MHz in the magnetic resonance spectrum and 6 MHz in the electric resonance spectrum.

$E_1 \cos \theta_{E_1} \cos(\omega_{E_1} t + \phi_{E_1})$, $E_y(t) = E_1 \sin \theta_{E_1} \cos(\omega_{E_1} t + \phi_{E_1})$ are the rf electric field's x and y components. By applying the rotating-wave approximation in the resonant condition $\omega_{E_1} = 2\gamma_e B_z$, the electron spin Hamiltonian in interaction picture is written as

$$H_1^I = \begin{pmatrix} 0 & 0 & H_{31}^* \\ 0 & 0 & 0 \\ H_{31} & 0 & 0 \end{pmatrix}, \quad (3)$$

where $H_{31} = -(i/2)d_{\perp} e^{-i(\theta_{E_1} - \phi_{E_1})} E_1$. Hence, the quantum transition between electron spin states $|\pm 1\rangle$ can be driven by a resonant rf electric field (see the Appendix). If the N-V center is prepared to the initial state $|-1\rangle$, the electron spin will oscillate between $m_s = \pm 1$. The projective

measurement of $m_s = -1$ after an evolution time of t is

$$S = \frac{1}{2} (1 + \cos(d_{\perp} E_1 t)), \quad (4)$$

where the angular Rabi frequency $d_{\perp} E_1$ is in proportion to the rf electric field amplitude E_1 . Taking into consideration the hyperfine interaction with the ^{15}N nuclear spin, there are now two electric transitions at frequencies of $2\gamma_e B_z \pm A$ [Fig. 1(b)].

In the experiment, we first measure the electric resonance spectrum. In the pulse sequence shown in Fig. 1(d), a 532-nm laser pulse and a short waiting time initialize the N-V center to $|0\rangle$. Then a MW π pulse flip the N-V center to $| -1\rangle$. Next, the spin state evolves in the presence of the rf electric field. Finally, another MW π pulse followed by a laser pulse is applied to measure the population of $| -1\rangle$. The PL of the N-V center is collected and normalized as the signal. When the rf is on resonance with the N-V center, the PL decreases. By sweeping the rf frequency, we observe the resonant peak at 108.24 and 114.30 MHz under the external magnetic field of $B_z = 19.87$ G. In the electric resonance spectrum, the splitting of 6 MHz, which is 2 times of the hyperfine splitting of the magnetic resonance spectrum, confirms that the peak is driven by the rf electric field [Figs. 1(e) and 1(f)].

III. AMPLITUDE MEASUREMENT

The measurement of the rf electric field's amplitude is based on the electrically driven Rabi oscillation. The pulse sequence is shown in Fig. 2(a). We adjust the external magnetic field such that the rf electric field is on resonance. After the electron spin is initialized to $| -1\rangle$, we vary the evolution time τ and measure the population on $| -1\rangle$. The Rabi oscillation is measured with total evolution time up to 500 μs [see Fig. 2(b)] and no visible decay is observed mostly because of the diluted ^{13}C spin bath noise [24]. The Rabi frequency of 74.89 kHz corresponds to the amplitude of 4405.4 ± 1.5 V cm^{-1} . Next, the slope detection [25] with the evolution time is fixed at 1 ms and the amplitude of the applied rf electric field is varied [see Fig. 2(c)]. According to the definition of sensitivity $\eta_E = \sigma_{\text{SN}}/dS$, where σ_{SN} is the standard deviation and $dS \propto d_{\perp} t e^{-\chi(t)}$ is the maximum slope where $e^{-\chi(t)}$ is the decoherence function that depends on the noise processes [25], a sensitivity of 265 $\text{V cm}^{-1} \text{ Hz}^{-1/2}$ is achieved. Furthermore, the minimum detectable electric field variation of 4.38 V cm^{-1} is achieved in the total measurement time of 500 s [see Fig. 2(d)]. Note that the experimental sensitivity is strongly limited by the shot noise of the photon counting. The corresponding quantum projection-noise-limited sensitivity is calculated to be 4.6 $\text{V cm}^{-1} \text{ Hz}^{-1/2}$ (see the Appendix for detailed discussion).

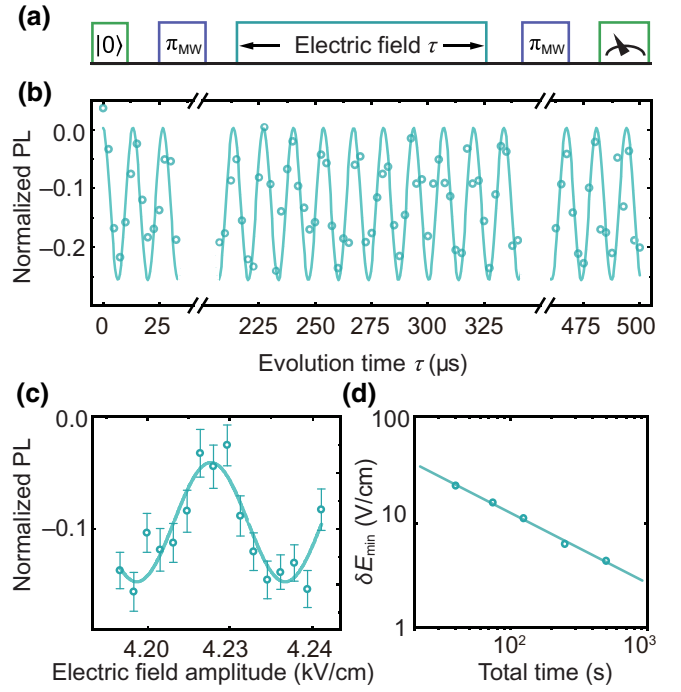


FIG. 2. Electrically driven Rabi oscillation and the amplitude sensing of rf electric fields. (a) The pulse sequence for electrically driven Rabi. (b) Rabi oscillation driven by a resonant rf electric field at 109.38 MHz. We fit the data to a sine curve. And the electric field amplitude is 4405.4 ± 1.5 V cm^{-1} . Only part of the data is shown for clarity (see the Appendix). (c) The slope detection of a 114.3-MHz electric field at a fixed evolution time of 1 ms, which shows a sinusoidal modulation of the normalized PL with respect to the amplitude of the electric field. (d) The measured minimally detected electric field uncertainty as a function of the total measurement time. The minimally detected electric field uncertainty reaches 4.38 V cm^{-1} in 500 s. The linear fit shows a sensitivity of 265 $\text{V cm}^{-1} \text{ Hz}^{-1/2}$ is achieved.

IV. PHASE MEASUREMENT

Next, we show that the measurement of relative phase between two rf electric fields can also be achieved using the electrically driven transition. We apply the electrically driven dynamical decoupling pulse sequence to measure the unknown relative phase between the signal (rfs) and the reference (rfr) [Fig. 3(a)]. rfs and rfr are two coherent rf electric fields at the same frequency. The N-V center is first initialized to $| -1\rangle$. Then, a $\pi/2$ pulse driven by rfr prepares the electron spin in superposition of $|\pm 1\rangle$. Next, multiple pairs of π pulses driven by rfs and rfr are repeated alternatively for N times. Because of the relative phase between the two rf electric fields, there will be an accumulated phase between $|\pm 1\rangle$. Finally, a rfs $\pi/2$ pulse is applied for projective measurement. The final signal is

$$S = \frac{1}{2} - \frac{\cos((2N+1)(\phi - \phi_{\text{ref}}))}{2}, \quad (5)$$

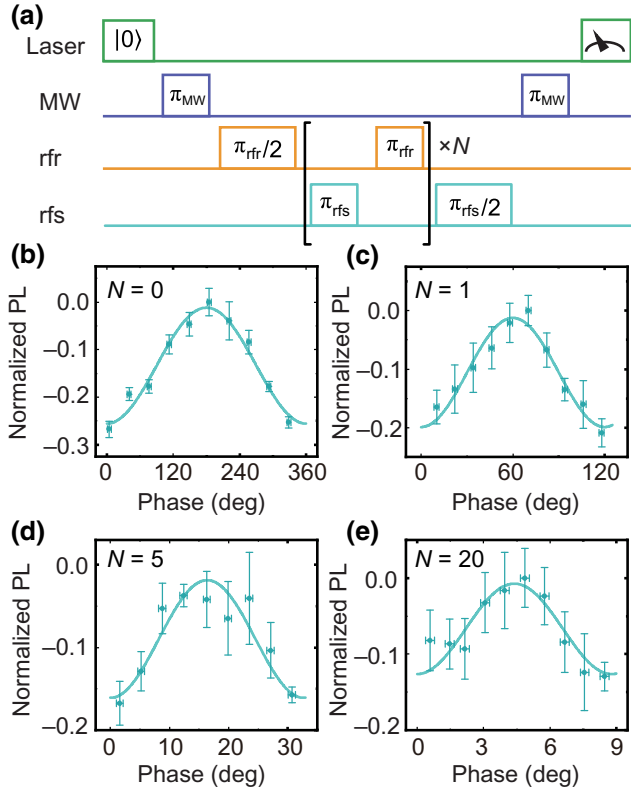


FIG. 3. Measurement of the relative phase between the rfs and the rfr. (a) The pulse sequence for phase measurement. (b)–(e) The normalized PL as a function of the phase of the rf reference with the repetition $N = 0, 1, 5,$ and 20 , respectively. The sine fits show the periods of $2\pi, 2\pi/3, 2\pi/11, 2\pi/41$. The x axes are shifted to make the axis starts from zero (see the Appendix).

in which ϕ is the phase of rfs and ϕ_{ref} is the phase of rfr (see the Appendix for details). The proof-of-principle experimental results of $N = 0, 1, 5, 20$ are shown in Figs. 3(b)–3(e). Increasing the number of π pairs N will shorten the oscillation period but the contrast decreases as well due to the decoherence. It gives the minimum standard deviation of phase measurement of 0.2° when $N = 20$.

V. SENSING OF THE RF ELECTROMAGNETIC COMPONENT

One advancement of our scheme is the capability to measure the magnetic or electric component of an rf field at the same place subsequently, which is a significant feature to realize the nanoscale rf fields imaging in the near-field region. Therefore, we analyze the effect of a rf field’s magnetic component on the measurement of the electric component. It is known that a rf magnetic field induces a small energy-level shift named Bloch-Siegert (BS) shift [26]:

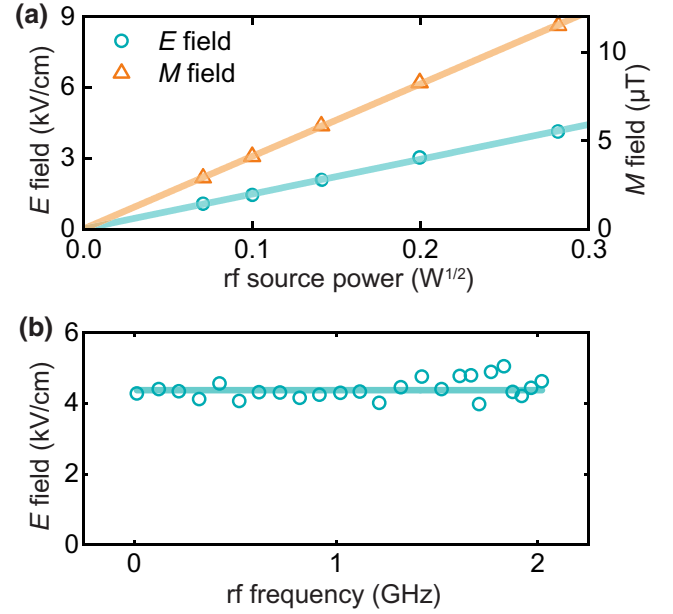


FIG. 4. Co-measurement of the electric and magnetic components of a rf field generated by a capacitive device shown in Fig. 1(a) and the electric response at a depth of several nanometers from the diamond surface. (a) The magnetic and electric components of a rf field at 1797.17 MHz with respect to different powers are illustrated. The linear fits give the intercepts of 5.8 V/cm and -35 nT for the electric and magnetic components, respectively. (b) The electric response from 13.85 MHz to 2.02 GHz. The solid line is a guideline at $E = 4379$ V/cm. The rf power keeps a constant during measurements.

$$\Delta\omega_{\text{BS}} = \frac{\gamma_e B_1^2}{8} \left(\frac{1}{f_+ - f} + \frac{2}{f_- + f} + \frac{2}{f_- - f} + \frac{1}{f_+ + f} \right), \quad (6)$$

where $f_{\pm} = D_{\text{GS}} \pm \gamma_e B_z$ and $f = 2\gamma_e B_z$. Normally, BS effect acts like a dc magnetic field. As a result, the BS shift has no influence on the amplitude and phase measurement because both Rabi and decoupling sequences are dc resistive. And the detuning caused by BS shift can be compensated by careful adjusting the external magnetic field based on the electric resonance spectrum. However, the effect of magnetic component cannot be neglected in the case where $f = 1913$ MHz or $f = 5740$ MHz due to the magnetic dipole transitions.

We demonstrate a simultaneous measurement of both components of a rf field at 1797.17 MHz using the conventional magnetically driven Rabi oscillation and electrically driven Rabi oscillation [see Fig. 4(a)]. We find that both magnetically and electrically driven Rabi frequencies, as a function of the applied ac voltages, show excellent linearity and zero intercepts, which enables the quantitative measurement of rf fields.

VI. FREQUENCY RESPONSE

In principle, the N- V center is able to sense the rf electric field with a wide frequency range. However, the influence of surface effect and the dielectric function at different frequencies are basic problems for electric field sensors in the solid-state system. Specifically, the electrometry based on the N- V center suffers from the surface-screening effect reported from dc to several tens of kilohertz [27,28], which limits the nanoscale applications using shallow N- V centers. Moreover, the variance of the dielectric function of diamond should be taken into account. It is predicted that at the rf frequency > 10 MHz, the response of rf fields will keep flat due to the flat dielectric constant [29]. Therefore, we vary the frequency of the rf field from 13.85 MHz to 2.02 GHz except 1913 MHz and measure the electrically driven Rabi oscillation [Fig. 4(b)]. We find that the detected electric field keeps approximately constant, which indicates that this is a suitable window for N- V -center-based electrometry.

VII. DISCUSSION

In conclusion, we realize the amplitude and phase sensing of rf electric fields based on the electrically driven transition of a shallow N- V center in diamond. The sensitivities of $265 \text{ V cm}^{-1} \text{ Hz}^{-1/2}$ for amplitude sensing and the standard deviation of 0.2° for phase detection are achieved. Meanwhile, we show that the N- V center can detect the electric and magnetic components of a rf field at the same place, which make it possible to co-measure rf electromagnetic fields in the near-field region. Although, it should be noted that the main limitation of the sensitivity is the shot noise due to the low PL rate (5 k/s) in our proof-of-principle experiments. As the quantum projection-noise-limited sensitivity for amplitude detection is $4.6 \text{ V cm}^{-1} \text{ Hz}^{-1/2}$, efficient optical structures and single-shot readout can be applied to approach this limit [30–32]. Based on the electrically driven transition, further study could combine the quantum coherent control such as quantum heterodyne protocol [33,34], spin-locking protocol [35] and pulsed Mollow absorption spectroscopy [36] for the precise amplitude, phase and frequency detection.

Combing our scheme with the scanning N- V center microscope (SNVM) [37,38], our approach can provide a rf imaging tool, which is easy to adopt and capable of electromagnetic field co-measurement with nanoscale resolution. Furthermore, this technique could benefit many studies of physics such as polar dynamics of ferroelectrics [39], and quantum microwave technology for electric manipulation of quantum systems [40–42].

The data that support the findings of this study are available from the corresponding author upon reasonable request.

ACKNOWLEDGMENTS

This work is supported by National Natural Science Foundation of China (Grants No. 81788101, No. 11874338, No. 51727808, No. T2125011, No. 12104447), the National Key R&D Program of China (Grant No. 2018YFA0306600), the Chinese Academy of Sciences (Grants No. XDC07000000, No. GJJSTD20200001, No. QYZDY-SSW-SLH004, No. ZDZBGCH2021002, No. 2021HSC-KPRD003), Innovation Program for Quantum Science and Technology (Grants No. 2021ZD0303204, No. 2021ZD0302200), Anhui Initiative in Quantum Information Technologies (Grant No. AHY050000), Hefei Comprehensive National Science Center, the Fundamental Research Funds for the Central Universities, China Postdoctoral Science Foundation (Grant No. 2020M671858).

This work is partially carried out at the USTC Center for Micro and Nanoscale Research and Fabrication.

APPENDIX A: DISCUSSION ABOUT THE ELECTRIC AND MAGNETIC COMPONENTS IN NEAR FIELD

Different from propagating electromagnetic fields in the far zone, there is no straightforward relationship between the electric and magnetic components of an electromagnetic wave in the near zone where the spatial scale is much smaller than the wavelength (10^{-3} to 1 m).

To understand the relationship between the electric and magnetic components of a rf field, we show the electric dipole radiation as a basic example.

We define d as the source dimensions, λ as the wavelength, and r as the distance to the source. The space is divided into three regions:

- (1) The near (static) field $d \ll r \ll \lambda$.
- (2) The intermediate (induction) field $d \ll r \sim \lambda$.
- (3) The far (radiation) field $d \ll \lambda \ll r$.

In the following, we discuss the radiation behavior in the near field and far field, where usually measurement performed.

The properties of electromagnetic radiation can be very different in the near (static) field and the far (radiation) field. The electric dipole radiation is an excellent example for analytical demonstration, whose vector potential $\vec{A}(\vec{x}, t)$ takes the following form under Lorenz gauge:

$$\vec{A}(\vec{x}) = -\frac{i\mu_0\omega}{4\pi} \vec{p} \frac{e^{ikr}}{r}, \quad (\text{A1})$$

where μ_0 is the vacuum permeability, ω is the angular frequency, k is the wave number, and \vec{p} is the electric dipole

moment. The corresponding electromagnetic field is

$$\vec{H} = \frac{ck^2}{4\pi} (\vec{n} \times \vec{p}) \frac{e^{ikr}}{r} \left(1 - \frac{1}{ikr}\right), \quad (\text{A2})$$

$$\vec{E} = \frac{1}{4\pi\epsilon_0} \left\{ k^2 (\vec{n} \times \vec{p}) \times \vec{n} \frac{e^{ikr}}{r} + [3\vec{n} (\vec{n} \cdot \vec{p}) - \vec{p}] \left(\frac{1}{r^3} - \frac{ik}{r^2} \right) e^{ikr} \right\}. \quad (\text{A3})$$

In the far field ($kr \gg 1$), the fields take on the limiting forms,

$$\vec{H}_f = \frac{ck^2}{4\pi} (\vec{n} \times \vec{p}) \frac{e^{ikr}}{r}, \quad (\text{A4})$$

$$\vec{E}_f = Z_0 \vec{H}_f \times \vec{n}, \quad (\text{A5})$$

which is the typical behavior of radiation fields. The electric field and the magnetic field have the relationship that $|E|/|H| = Z_0$, where $Z_0 = 120\pi\Omega$ is the vacuum impedance. So, we can measure one of the electric or magnetic component of a rf field to determine the other one in the far field.

In the near field, the fields approach

$$\vec{H}_n = \frac{i\omega}{4\pi} (\vec{n} \times \vec{p}) \frac{1}{r^2}, \quad (\text{A6})$$

$$\vec{E}_n = \frac{1}{4\pi\epsilon_0} [3\vec{n} (\vec{n} \cdot \vec{p}) - \vec{p}] \frac{1}{r^3}. \quad (\text{A7})$$

It appears no straightforward relationship between the two components. The change in the parameters such as ϵ_0 will not affect the magnetic field. Of note, the estimation of the ratio $|\vec{E}|/|\vec{H}| = Z_0/kr$ shows that the fields in the near field are dominantly electric in nature. The magnetic field vanishes.

From the example of electric dipole radiation, we show the fact that electric and magnetic fields in the near field are independent quantities. Thus, we cannot infer the distribution of electric field from the magnetic field because of the complex geometry and different material properties. Besides, the fact is also proved by experiments [6]. Therefore, combining the sensing of rf electric fields demonstrated in this work and the detection of rf magnetic fields achieved in previous works should enable complete analysis of a near-zone rf field.

APPENDIX B: COMPARISON OF ELECTRIC FIELD SENSORS

The electric field sensing is a basic tool in current science and technology. The areas of fundamental physics, material science, integrated circuits and devices and quantum technology would greatly benefit from the development of a high-bandwidth, nanoscale electric field

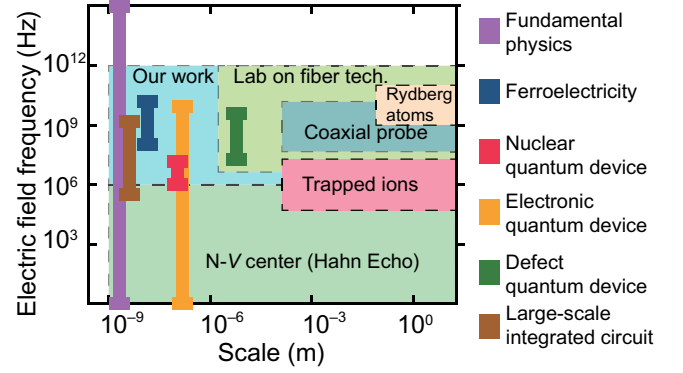


FIG. 5. Comparison of electric field sensors in sensor scale, frequency range, and applications.

sensor. The specific potential applications include the Maxwell equations and framework for electromagnetism at nanoscale, the microwave tunable ferroelectricity, the electromagnetic sensing of basic electronic devices, such as transistors in CPU and FPGA, and the characterization of the quantum devices. The development of such sensors would attract broad interest in these fields. We note that there is no straightforward relationship between the magnetic field and electric field in the rf near-field region (see the previous section for details). So, the co-measurement of the electric and magnetic field is on demand to gain full information of the rf radiation in the applications above. We present the potential applications in Fig. 5.

Many kinds of sensors are developed for the rf electric field sensing. The Rydberg atoms and the two-dimensional trapped-ion crystals are developed as the most sensitive quantum rf electric field sensor but with a spatial resolution of sub-mm or centimeter scale. The fiber optics and the open-ended coaxial probe are commonly used electric field sensors but only provide microscale spatial resolution even with the state-of-the-art technology. The properties of these sensors are listed in Table I. We also present the electric field sensors in the scale and bandwidth dimensions in Fig. 5 and Table I.

In recent decades, the N-V center is being developed as a magnetic field sensor as well as an electric field sensor with nanoscale spatial resolution. The electric field sensing based on the N-V center is demonstrated using the spin-echo pulse sequence, the ODMR spectrum, and the dressed state transitions. However, to date, these methods are not suitable for the measurement of rf electric fields. For example, in the spin-echo pulse sequence, for the $\nu > 1$ GHz, the π pulses should be spaced with the interval of about 0.5 ns and the length of the π pulse should be much less than 0.5 ns, which is almost impossible under current microwave technology. But in our method, the electrically driven transition is tuned to be on resonant with the rf electric field by the external biased magnetic field, which makes it possible to measure even THz electric

TABLE I. Comparison of electric field sensors.

Sensor type	Size (m)	Sensitivity	Frequency
Rydberg atom [10]	10^{-2}	$55 \text{ nV cm}^{-1} \text{ Hz}^{-1/2}$	10 GHz, 1-500 GHz in principle
Trapped ions [13]	10^{-4}	$2.4 \text{ nV cm}^{-1} \text{ Hz}^{-1/2}$	1.59 MHz
Lab-on-fiber tech. [9]	10^{-5}	$0.32 \text{ V cm}^{-1} \text{ Hz}^{-1/2}$	10 MHz, Up to THz in principle
N- V (Hahn echo) [19]	10^{-9}	$202 \text{ V cm}^{-1} \text{ Hz}^{-1/2}$	Up to few MHz
This work	10^{-9}	$265 \text{ V cm}^{-1} \text{ Hz}^{-1/2}$	0.013-2.02 GHz, Up to THz under 17.9 T in principle

field. Moreover, our method allows the co-measurement of the magnetic and electric field, which cannot be achieved in other existing methods. Finally, the usage of the shallow N- V center makes our method ready for the sensing of the rf electric field and magnetic field from the extensive samples.

APPENDIX C: EXPERIMENTAL SETUP

Our experiments are carried out on a home-built optical detected magnetic resonance (ODMR) platform. The ODMR platform contains the confocal setup, the delivery of rf and the experiment control.

The confocal setup is for optical access and detection of single N- V centers. Using a microscope objective (Olympus LUCPLANFL 60 \times), we locate single N- V centers and perform optical polarization via a 532-nm laser, which is modulated by double passing an acousto-optical modulator (Gooch & Housego 3200-121). The spin-dependent PL of N- V centers is separated by a dichroic filter. Then we collect the PL photons using a photodetector (PD) (Excelitas Technologies SPCM-AQRH-13). The output signal of the PD are recorded by a counter (National Instrument PCIe-6612).

As shown in Figs. 6 and 7, we apply ac voltages on the top left pair of electrodes. A rf source (Stanford SG386)

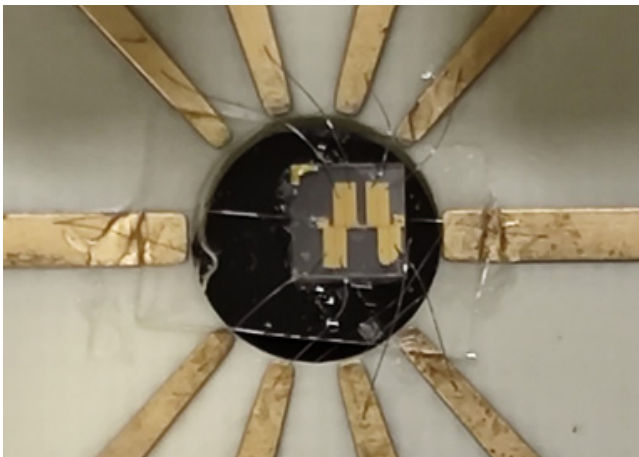


FIG. 6. Photo of the diamond. The stripline generates MW to initialize and readout the electron spin state. Two electrodes generate the rf electric field and magnetic field to be measured.

is applied to generate the ac voltage in the measurement of amplitude. And the same rf source is marked as rfs in the phase measurement when another rf source (Ceyear 1435b-v) is applied to generate rfr. The rfs and rfr share a same timeclock. Two MW switches control the on and off of the applied rf (Minicircuits ZASWA-2-50DR+). And the two rfs share the same SMA port connected to the electrodes. The MW applied for spin-state initialization and projective readout is radiated by the stripline. The MW is generated by a rf source (Stanford SG386). Through a MW switch (Minicircuits ZASWA-2-50DR+), the MW is amplified by an amplifier (Minicircuits ZHL-16W-43s+) and delivered to the stripline.

The experimental flow is controlled by a pulse blaster (PB) (Spincore PulseBlasterESR-PRO-250). To synchronize the devices at an accuracy of nanoseconds, we use the PB to control the switch of rf and MW, the length of laser pulse and the collection of PL photons.

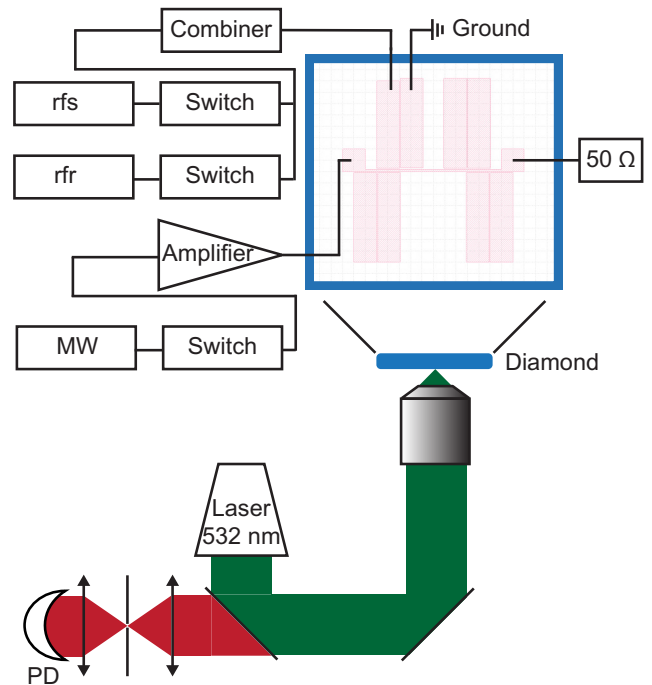


FIG. 7. Experimental setup including the confocal microscope and the MW and rf delivery.

APPENDIX D: ELECTRICALLY DRIVEN RABI EVOLUTION FOR AMPLITUDE DETECTION

The quantum state evolution at the presence of a resonant rf electric field is analyzed in the following steps.

First, the Hamiltonian of the electron spin is

$$H_{\text{GS}} = D_{\text{GS}}S_z^2 + \gamma_e B_z S_z + H_{\text{rf}}^E, \quad (\text{D1})$$

where D_{GS} is the zero-field splitting, γ_e and γ_N are the gyromagnetic ratios for electron spin and the ^{15}N nuclear spin, $\mathbf{S} = (S_x, S_y, S_z)$ are the electron spin-1 operators, $d_{\perp} = 17 \pm 3 \text{ HzcmV}^{-1}$ is the N-V centers' nonaxial electric dipole moment. And the expression of H_{rf}^E is in Eq. (2).

Second, to switch to the interaction picture, we set the static Hamiltonian H_0^S to be

$$H_0^S = \lambda (D_{\text{GS}}S_z^2 + \gamma_e B_z S_z), \quad (\text{D2})$$

where λ is a parameter. The dynamic Hamiltonian is

$$H_1^S = H_{\text{GS}} - H_0^S. \quad (\text{D3})$$

After splitting the static and the dynamic part, we transform the Hamiltonian to the interaction picture, where

$$H_1^I = e^{iH_0^S t} H_1^S e^{-iH_0^S t}. \quad (\text{D4})$$

Let $\lambda = \omega_{E_1}/(2\gamma B_z)$, we eliminate the $2\omega_{E_1}$ time-dependent items by applying the rotational-wave approximation (RWA). The evolution Hamiltonian at presence of a resonant rf electric field ($\omega_{E_1} = 2\gamma_e B_z$) is

$$H_1^I = \begin{pmatrix} 0 & 0 & \frac{i}{2}d_{\perp}E_1 e^{i(\theta_{E_1} - \phi_{E_1})} \\ 0 & 0 & 0 \\ -\frac{i}{2}d_{\perp}E_1 e^{i(\phi_{E_1} - \theta_{E_1})} & 0 & 0 \end{pmatrix}. \quad (\text{D5})$$

And the evolution operator is

$$U_1^I = e^{-iH_1^I t}. \quad (\text{D6})$$

According to the evolution operator (D6), the electrically driven Rabi oscillation can be observed when the spin is initialized to $m_s = -1$,

$$U_1^I | -1 \rangle = e^{i(\theta_{E_1} - \phi_{E_1})} \sin \frac{d_{\perp} E_1 t}{2} | +1 \rangle + \cos \frac{d_{\perp} E_1 t}{2} | -1 \rangle \quad (\text{D7})$$

after the projective measurement,

$$S = |\langle -1 | U_1^I | -1 \rangle|^2 = \frac{1}{2} (1 + \cos d_{\perp} E_1 t). \quad (\text{D8})$$

APPENDIX E: DATA FOR ELECTRICALLY DRIVEN RABI

In the section, we show the complete data of the 500- μs electrically driven Rabi oscillation (Fig. 8), which is partly illustrated in the main text for clarity.

APPENDIX F: QUANTUM-PROJECTION-NOISE-LIMITED SENSITIVITY

The signal of amplitude detection is

$$S = \frac{1}{2} (1 + \cos (d_{\perp} E_1 t)), \quad (\text{F1})$$

where in slope detection we fix the evolution time to t at which $\cos (d_{\perp} E_1 t) = 0$ to achieve maximum slope. Thus,

$$\delta S = \frac{1}{2} (1 + \cos (d_{\perp} (E_1 + \delta E_1) t)) - \frac{1}{2} = \pm \frac{1}{2} d_{\perp} t \delta E_1. \quad (\text{F2})$$

Next we calculate the quantum projection-noise-limited sensitivity.

The quantum projection noise is brought by the projective measurement of a superposition state, which is unavoidable for slope detection. According to the binomial distribution, the standard deviation is

$$\sigma^2 = \frac{1}{N} p(1-p), \quad (\text{F3})$$

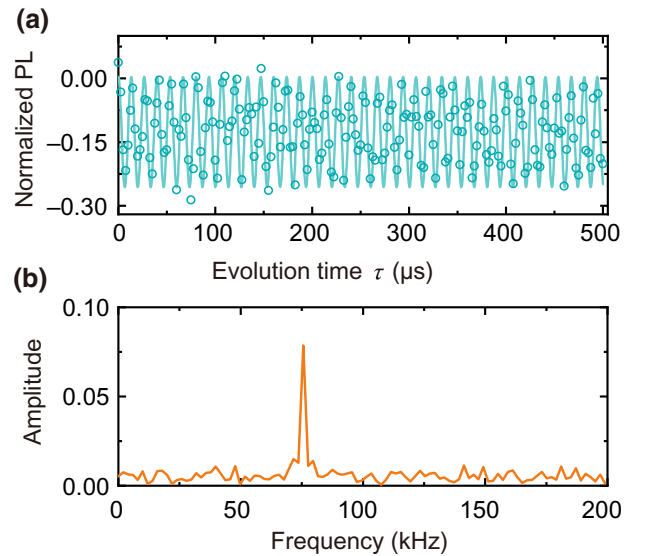


FIG. 8. (a) Raw data of the 500- μs electrically driven Rabi oscillation. (b) The Fourier transformation of the data in (a).

where $p = 0.5$ is the probability in our case. Therefore, the quantum projection noise is

$$\sigma = \frac{1}{2\sqrt{N}}. \quad (\text{F4})$$

The decoherence can be phenomenologically described using an exponential decay.

$$\delta S_{\text{obs}} = \delta S e^{-\chi(t)}, \quad (\text{F5})$$

where the $\chi(t)$ is the decoherence rate, and the δS_{obs} is the observed signal.

The signal-to-noise ratio is

$$\frac{\delta S_{\text{obs}}}{\sigma} = \frac{\frac{1}{2}d_{\perp}t\delta E_1 e^{-\chi(t)}}{\frac{1}{2\sqrt{N}}} = d_{\perp}t\delta E_1 e^{-\chi(t)}\sqrt{N}, \quad (\text{F6})$$

where sensitivity is the minimally detected electric field at a unit time for a unit signal-to-noise ratio. Thus,

$$1 = d_{\perp}t\delta E_1 e^{-\chi(t)}\sqrt{N}. \quad (\text{F7})$$

And the sensitivity is

$$\delta E_1 = \frac{e^{\chi(t)}}{d_{\perp}}\sqrt{\frac{1}{t}}. \quad (\text{F8})$$

We estimate the quantum projection-noise-limited sensitivity at 1 ms to be $4.579 \text{ V cm}^{-1} \text{ Hz}^{-1/2}$, where $e^{\chi(t)} = 2.46$ is measured by experiment.

APPENDIX G: PHASE DETECTION

As shown in previous sections, the evolution operator of the electron spin in the presence of a rf field is a function of evolution time. We denote two operators of fixed evolution times,

$$U_{\frac{\pi}{2}}^t = U_1^t \left(t = \frac{\pi}{2} \frac{1}{d_{\perp}E_1} \right), \quad (\text{G1})$$

and

$$U_{\pi}^t = U_1^t \left(t = \pi \frac{1}{d_{\perp}E_1} \right). \quad (\text{G2})$$

The final signal of the electron spin is

$$\left| \langle -1 | U_{\frac{\pi}{2}}^t(\phi) \prod_{n=0}^N [U_{\pi}^t(\phi_{\text{ref}}) U_{\pi}^t(\phi)] U_{\frac{\pi}{2}}^t(\phi_{\text{ref}}) | -1 \rangle \right|^2 \quad (\text{G3})$$

in which ϕ is the phase of rfs electric field and ϕ_{ref} is the phase of rfr electric field. And the result is shown as Eq. (5) in the main text.

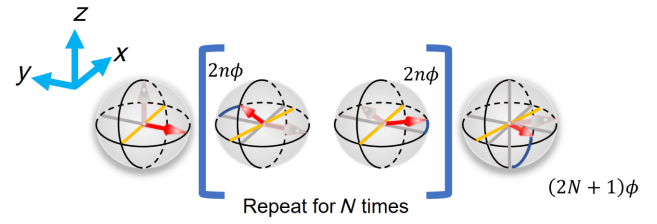


FIG. 9. Evolution of the Bloch vector for phase measurement. In the figure, the gray arrow is the last position before the evolution while the red arrow is the position after rotation. The yellow axis in the sphere is the rotating axis for each step. The angle is marked using the blue arc.

Considering the complication of operator computation, we show the visualization of evolutions by mapping the state transformation to rotations of the Bloch vector in Fig. 9. The U_1^t corresponds to the rotation about an axis in the x - y plane with azimuthal angles of ϕ or ϕ_{ref} . Specifically, $U_{\pi/2}^t$ and U_{π}^t correspond to the rotation angle of $\pi/2$ and π . We demonstrate an example of rotation assuming $\phi_{\text{ref}} = 0$. The Bloch vector is first polarized to $(0, 0, 1)$. After the $U_{\pi/2}^t$ transformation driven by rfr, the Bloch vector and the negative y axis coincide. And the Bloch vector rotates to $(-\sin(2\phi), \cos(2\phi), 0)$ after the U_{π}^t driven by rfs. Similarly, the Bloch vector rotates to $(-\sin(2\phi), -\cos(2\phi), 0)$ after the U_{π}^t driven by rfr. By each application of the U_{π}^t pairs, the Bloch vectors' angle to the y axis increases 2ϕ , which is $(-\sin(2n\phi), -\cos(2n\phi), 0)$. After the last rotation of $U_{\pi/2}^t$ driven by rfs, the Bloch vector has an angle of $(2N+1)\phi$ to the negative z axis, which is the same as the result derived by operator computation.

APPENDIX H: ALIGNMENT OF RELATIVE PHASE IN PHASE DETECTION

To observe the PL signal with respect to the relative phase in the phase measurement, we keep the phase of the rfr and vary the phase of the rfs. According to the expression (5), the signal reaches the minimum point when ϕ equals ϕ_{ref} . Because of the nonzero initial phase due to the rf sources, the measured signal is horizontally translated. We shift the x axis to align the start of the relative phase to zero. The shift is done by following judgement: if the relative value is smaller than the zero position, a period is added to the raw value. And for those relative phase greater than the zero position, we keep the raw relative phase.

APPENDIX I: SENSITIVITY FOR PHASE MEASUREMENT

We measure the sensitivity of the phase detection following the same protocol as the amplitude measurement. As shown in Fig. 10, we achieve the sensitivity of $25.7^\circ/\sqrt{\text{Hz}}$ when $N = 20$.

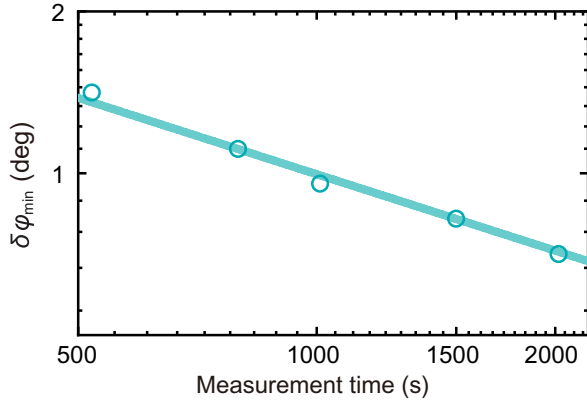


FIG. 10. The measured minimally detected phase uncertainty as a function of the total measurement time.

APPENDIX J: INFLUENCE OF DETUNING AND AMPLITUDE NOISE ON PHASE MEASUREMENT

We reconsider the influence of the error of frequency and amplitude of the rf field and show the detailed theoretical calculation. We suppose that the signal and reference rf are at the same frequency. Otherwise, the relative phase between two incoherent rfs is meaningless. The detuning between the rf frequency and the resonant frequency causes off resonance. The inaccurate prior knowledge of the signal amplitude results in the inaccurate $\pi/2$ and π pulse length. For analysis, we simply add the detuning $\delta\omega_e$ on the rf frequency and δT_s and δT_r on the period of the Rabi oscillation of signal and reference, respectively. We compute the Hamiltonian in the S_z representation with the error of detuning and the error of $\pi/2$, π length in the Rabi experiments. As the calculation in the phase measurement, we follow a similar procedure.

(1) The time-independent part and time-dependent part of the Hamiltonian in the Schrödinger picture.

$$H_0 = \lambda (D_{GS} S_z^2 + \gamma_e B_z S_z), \quad (J1)$$

$$H_1^S = H_{GS} - H_0, \quad (J2)$$

where H_{GS} is the ground spin-state Hamiltonian in Eq. (D1).

(2) Switch to the interaction picture.

$$H_1^I = \exp(iH_0 t) H_1^S \exp(-iH_0 t). \quad (J3)$$

(3) Let $\lambda = \omega_e / (2\gamma B_z)$, and perform the RWA.

(4) Different from the resonance circumstance, a small detuning is added to figure out the influence of the frequency error, which makes $\omega_e = 2\gamma B_z + \delta\omega_e$.

(5) H_1^I is now time independent, we can write the evolution operator

$$U_1^I = \exp(-iH_1^I t). \quad (J4)$$

And we derive the Rabi oscillation based on the evolution operator

$$S_{\text{Rabi}} = \frac{d_{\perp}^2 E_1^2 + 2\delta\omega_e^2 + d_{\perp}^2 E_1^2 \cos\left(t\sqrt{d_{\perp}^2 E_1^2 + \delta\omega_e^2}\right)}{2d_{\perp}^2 E_1^2 + 2\delta\omega_e^2}. \quad (J5)$$

Through the expression, we find the period of the Rabi, where an error δT of the Rabi period T in the expression represents the estimation of the amplitude error contribution

$$T_r = \delta T_r + 2\pi / \sqrt{d_{\perp}^2 E_{1r}^2 + \delta\omega_e^2}, \quad (J6)$$

$$T_s = \delta T_s + 2\pi / \sqrt{d_{\perp}^2 E_{1s}^2 + \delta\omega_e^2}, \quad (J7)$$

where δT_s and δT_r are the error of Rabi period for rf signal and reference, E_{1s} and E_{1r} are the electric field amplitudes for rf signal and reference.

And the signal of phase measurements is

$$S = \left| \langle 0 | U_m U_{1\frac{T_r}{4}}^I(\phi_e) \prod_{n=0}^N \left[U_{1\frac{T_s}{2}}^I(0) U_{1\frac{T_r}{2}}^I(\phi_e) \right] \times U_{1\frac{T_s}{4}}^I(0) U_m | 0 \rangle \right|^2, \quad (J8)$$

where the U_m is the flip of population on $|0\rangle$ and $|-1\rangle$ using the magnetically driven pulse. And we assume the magnetically driven pulse is on resonance. Thus,

$$U_m(t, t_0) = e^{i(\delta\omega_e/2\gamma B_z)H_0 t} e^{-iH_1 t} e^{-i(\delta\omega_e/2\gamma B_z)H_0 t} \times e^{i(\delta\omega_e/2\gamma B_z)H_0 t_0} e^{iH_1 t_0} e^{-i(\delta\omega_e/2\gamma B_z)H_0 t_0}. \quad (J9)$$

Calculating S with the derived U_m and U_1^I , we can have the following expression of the phase measurement signal in first order:

$$\begin{aligned} & \left| \langle 0 | U_m U_{1\pi/2}^I(\phi_e) \prod_{n=0}^N \left[U_{1\pi}^I(0) U_{1\pi}^I(\phi_e) \right] U_{1\pi/2}^I(0) U_m | 0 \rangle \right|^2 \\ & \approx \frac{1}{2} - \frac{1}{2} \cos[(2N+1)\phi_e] + \left(\frac{\delta\omega_e}{2d_{\perp}E_{1s}} + \frac{\delta\omega_e}{2d_{\perp}E_{1r}} \right) \sin[(2N+1)\phi_e] + \mathcal{O}(\delta\omega_e^2) + \mathcal{O}(\delta T_s^2) + \mathcal{O}(\delta T_r^2) \end{aligned} \quad (J10)$$

where \mathcal{O} represents high-order contributions.

With the Taylor series,

$$\cos(k\phi_e + \Delta) = \cos(k\phi_e) - \sin(k\phi_e)\Delta + \mathcal{O}(\Delta^2). \quad (\text{J11})$$

We can see the influence of the detuning and the error of amplitude on the result.

$$S = \frac{1}{2} - \frac{1}{2} \cos \left[(2N+1)\phi_e + \delta\omega_e \left(\frac{1}{2d_{\perp}E_{1s}} + \frac{1}{2d_{\perp}E_{1r}} \right) \right] + \mathcal{O}(\delta\omega_e^2) + \mathcal{O}(\delta T_1^2) + \mathcal{O}(\delta T_2^2). \quad (\text{J12})$$

According to the result, the effect of the error of amplitude or Rabi period is of the second order with respect to the detuning, which can be neglected in our further discussion. And the effect of detuning depends on two factors: the electric field power and the number of π pairs can depress the error. Based on the results of our proof-of-principle experiments, we estimate the error using the formula

$$\delta\phi_e = \delta\omega_e \left(\frac{1}{2d_{\perp}E_{1s}} + \frac{1}{2d_{\perp}E_{1r}} \right) / (2N+1) = 0.31^\circ. \quad (\text{J13})$$

According to this result, we can define $\delta\phi_e$ as the inaccuracy to the real value. $\delta\phi_e$ mainly depends on two factors: the electric field amplitude and the number of π pulse pairs. The effect of the error of the rf amplitude is of the second order with respect to the experimental result. In our experiment, we estimate the inaccuracy is 0.31° , which is the same order with the standard deviation 0.2° .

APPENDIX K: ANALYSIS OF THE DECAY IN PHASE MEASUREMENT

In the phase measurement, there is a fast decay process compared to the Rabi oscillation. The fast decay can be explained by the charge instability of N-V center.

As previously studied [43], the charge instability is related to the last time when the diamond is acid cleaned. The total experiment lasted for 6 months. The last fabricating process of the coplanar device is the cleaning of the photoresist by the ultrapure developer. Shortly after that, we measure the Rabi oscillation and obtain a contrast of about 0.3. During the experiment, the diamond is exposed in the ambient condition so the charge related environment on the diamond surface, such as the chemical bond, the charge density, and distribution have changed and affect the charge property of the N-V center. The phase measurement is the last experiment so the charge environment is very different with the Rabi oscillation at the very beginning. In the phase measurement, we perform Figs. 3(b)–3(e) with different N one by one. The average dark time is different with different N and the probability of N-V⁻ and N-V⁰ is different. Based on the Ref. [43], the

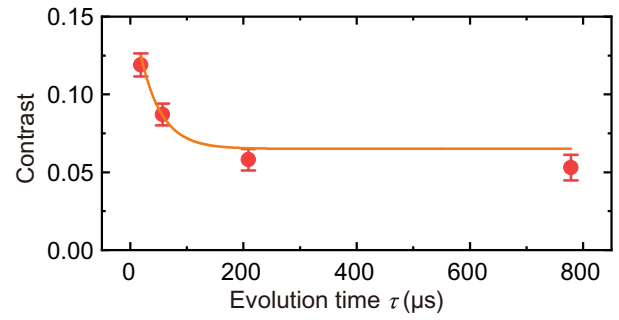


FIG. 11. Decay of phase measurement fit.

N-V⁻ probability ρ^- is a function of the dark time in pulse measurement. The decay can be well described using the model

$$\rho^-(t) = \rho^-(0)[1 - A(1 - e^{-\Gamma ct})]. \quad (\text{K1})$$

Using the model, the decay of phase measurement is fitted in Fig. 11.

- [1] Y. Yang, D. Zhu, W. Yan, A. Agarwal, M. Zheng, J. D. Joannopoulos, P. Lalanne, T. Christensen, K. K. Berggren, and M. Soljačić, A general theoretical and experimental framework for nanoscale electromagnetism, *Nature* **576**, 248 (2019).
- [2] C. T. Hill, Axion induced oscillating electric dipole moment of the electron, *Phys. Rev. D* **93**, 025007 (2016).
- [3] Z. Gu, S. Pandya, A. Samanta, S. Liu, G. Xiao, C. J. G. Meyers, A. R. Damodaran, H. Barak, A. Dasgupta, S. Saremi, A. Polemi, L. Wu, A. A. Podpirka, A. Will-Cole, C. J. Hawley, P. K. Davies, R. A. York, I. Grinberg, L. W. Martin, and J. E. Spanier, Resonant domain-wall-enhanced tunable microwave ferroelectrics, *Nature* **560**, 622 (2018).
- [4] J. H. Haeni, P. Irvin, W. Chang, R. Uecker, P. Reiche, Y. L. Li, S. Choudhury, W. Tian, M. E. Hawley, B. Craigo, A. K. Tagantsev, X. Q. Pan, S. K. Streiffer, L. Q. Chen, S. W. Kirchoefer, J. Levy, and D. G. Schlom, Room-temperature ferroelectricity in strained SrTiO₃, *Nature* **430**, 758 (2004).
- [5] J. D. Jackson, Classical electrodynamics, 3rd edition (1998).
- [6] W. Shao, W. Fang, Y. Huang, G. Li, L. Wang, Z. He, E. Shao, Y. Guo, Y. En, and B. Yao, Simultaneous measurement of electric and magnetic fields with a dual probe for efficient near-field scanning, *IEEE Trans. Antennas Propag.* **67**, 2859 (2019).
- [7] T. Dubois, S. Jarrix, A. Penarier, P. Nouvel, D. Gasquet, L. Chusseau, and B. Azais, Near-field electromagnetic characterization and perturbation of logic circuits, *IEEE Trans. Instrum. Meas.* **57**, 2398 (2008).
- [8] G. Kostovski, P. R. Stoddart, and A. Mitchell, The optical fiber tip: An inherently light-coupled microscopic platform for micro- and nanotechnologies, *Adv. Mater.* **26**, 3798 (2014).

- [9] V. Calero, M.-A. Suarez, R. Salut, F. Baida, A. Caspar, F. Behague, N. Courjal, L. Galtier, L. Gillette, L. Duvillaret, G. Gaborit, and M.-P. Bernal, An ultra wideband-high spatial resolution-compact electric field sensor based on lab-on-fiber technology, *Sci. Rep.* **9**, 8058 (2019).
- [10] M. Jing, Y. Hu, J. Ma, H. Zhang, L. Zhang, L. Xiao, and S. Jia, Atomic superheterodyne receiver based on microwave-dressed Rydberg spectroscopy, *Nat. Phys.* **16**, 911 (2020).
- [11] J. A. Sedlacek, A. Schwettmann, H. Kubler, and J. P. Shaffer, Atom-Based Vector Microwave Electrometry using Rubidium Rydberg Atoms in a Vapor Cell, *Phys. Rev. Lett.* **111**, 063001 (2013).
- [12] J. A. Sedlacek, A. Schwettmann, H. Kübler, R. Löw, T. Pfau, and J. P. Shaffer, Microwave electrometry with Rydberg atoms in a vapour cell using bright atomic resonances, *Nat. Phys.* **8**, 819 (2012).
- [13] K. A. Gilmore, M. Affölder, R. J. Lewis-Swan, D. Barberena, E. Jordan, A. M. Rey, and J. J. Bollinger, Quantum-enhanced sensing of displacements and electric fields with two-dimensional trapped-ion crystals, *Science* **373**, 673 (2021).
- [14] M. W. Doherty, N. B. Manson, P. Delaney, F. Jelezko, J. Wrachtrup, and L. C. L. Hollenberg, The nitrogen-vacancy colour centre in diamond, *Phys. Rep.* **528**, 1 (2013).
- [15] J. F. Barry, J. M. Schloss, E. Bauch, M. J. Turner, C. A. Hart, L. M. Pham, and R. L. Walsworth, Sensitivity optimization for NV-diamond magnetometry, *Rev. Mod. Phys.* **92**, 015004 (2020).
- [16] P. Wang, Z. Yuan, P. Huang, X. Rong, M. Wang, X. Xu, C. Duan, C. Ju, F. Shi, and J. Du, High-resolution vector microwave magnetometry based on solid-state spins in diamond, *Nat. Commun.* **6**, 6631 (2015).
- [17] J. R. Maze, P. L. Stanwix, J. S. Hodges, S. Hong, J. M. Taylor, P. Cappellaro, L. Jiang, M. V. G. Dutt, E. Togan, A. S. Zibrov, A. Yacoby, R. L. Walsworth, and M. D. Lukin, Nanoscale magnetic sensing with an individual electronic spin in diamond, *Nature* **455**, 644 (2008).
- [18] G. Balasubramanian, I. Y. Chan, R. Kolesov, M. Al-Hmoud, J. Tisler, C. Shin, C. Kim, A. Wojcik, P. R. Hemmer, A. Krueger, T. Hanke, A. Leitenstorfer, R. Bratschkitsch, F. Jelezko, and J. Wrachtrup, Nanoscale imaging magnetometry with diamond spins under ambient conditions, *Nature* **455**, 648 (2008).
- [19] F. Dolde, H. Fedder, M. W. Doherty, T. Nöbauer, F. Rempp, G. Balasubramanian, T. Wolf, F. Reinhard, L. C. L. Hollenberg, F. Jelezko, and J. Wrachtrup, Electric-field sensing using single diamond spins, *Nat. Phys.* **7**, 459 (2011).
- [20] M. Block, B. Kobrin, A. Jarmola, S. Hsieh, C. Zu, N. L. Figueroa, V. M. Acosta, J. Minguzzi, J. R. Maze, D. Budker, and N. Y. Yao, Optically Enhanced Electric Field Sensing using Nitrogen-Vacancy Ensembles, *Phys. Rev. Appl.* **16**, 024024 (2021).
- [21] K. Bian, W. Zheng, X. Zeng, X. Chen, R. Stöhr, A. Denisenko, S. Yang, J. Wrachtrup, and Y. Jiang, Nanoscale electric-field imaging based on a quantum sensor and its charge-state control under ambient condition, *Nat. Commun.* **12**, 2457 (2021).
- [22] M. S. J. Barson, L. M. Oberg, L. P. McGuinness, A. Denisenko, N. B. Manson, J. Wrachtrup, and M. W. Doherty, Nanoscale vector electric field imaging using a single electron spin, *Nano Lett.* **21**, 2962 (2021).
- [23] L. M. Pham, S. J. DeVience, F. Casola, I. Lovchinsky, A. O. Sushkov, E. Bersin, J. Lee, E. Urbach, P. Cappellaro, H. Park, A. Yacoby, M. Lukin, and R. L. Walsworth, NMR technique for determining the depth of shallow nitrogen-vacancy centers in diamond, *Phys. Rev. B* **93**, 045425 (2016).
- [24] G. Balasubramanian, P. Neumann, D. Twitchen, M. Markham, R. Kolesov, N. Mizuochi, J. Isoya, J. Achard, J. Beck, J. Tisler, V. Jacques, P. R. Hemmer, F. Jelezko, and J. Wrachtrup, Ultralong spin coherence time in isotopically engineered diamond, *Nat. Mater.* **8**, 383 (2009).
- [25] C. L. Degen, F. Reinhard, and P. Cappellaro, Quantum sensing, *Rev. Mod. Phys.* **89**, 035002 (2017).
- [26] R. Li, C.-J. Wang, Z. Cheng, P. Wang, Y. Wang, C. Duan, H. Liu, F. Shi, and J. Du, Wideband microwave magnetometry using a nitrogen-vacancy center in diamond, *Phys. Rev. A* **99**, 062328 (2019).
- [27] L. M. Oberg, M. O. de Vries, L. Hanlon, K. Strazdins, M. S. J. Barson, M. W. Doherty, and J. Wrachtrup, Solution to Electric Field Screening in Diamond Quantum Electrometers, *Phys. Rev. Appl.* **14**, 014085 (2020).
- [28] Z. Qiu, A. Hamo, U. Vool, T. X. Zhou, and A. Yacoby, Nanoscale electric field imaging with an ambient scanning quantum sensor microscope (2022), *ArXiv:2205.03952*.
- [29] A. Ibarra, M. González, R. Vila, and J. Mollá, Wide frequency dielectric properties of CVD diamond, *Diam. Relat. Mater.* **6**, 856 (1997).
- [30] Q. Zhang, Y. Guo, W. Ji, M. Wang, J. Yin, F. Kong, Y. Lin, C. Yin, F. Shi, Y. Wang, and J. Du, High-fidelity single-shot readout of single electron spin in diamond with spin-to-charge conversion, *Nat. Commun.* **12**, 1529 (2021).
- [31] P. Neumann, J. Beck, M. Steiner, F. Rempp, H. Fedder, P. R. Hemmer, J. Wrachtrup, and F. Jelezko, Single-shot readout of a single nuclear spin, *Science* **329**, 542 (2010).
- [32] C. Bonato, M. S. Blok, H. T. Dinani, D. W. Berry, M. L. Markham, D. J. Twitchen, and R. Hanson, Optimized quantum sensing with a single electron spin using real-time adaptive measurements, *Nat. Nanotechnol.* **11**, 247 (2016).
- [33] S. Schmitt, T. Gefen, F. M. Stürner, T. Unden, G. Wolff, C. Müller, J. Scheuer, B. Naydenov, M. Markham, S. Pezagna, J. Meijer, I. Schwarz, M. Plenio, A. Retzker, L. P. McGuinness, and F. Jelezko, Submillihertz magnetic spectroscopy performed with a nanoscale quantum sensor, *Science* **356**, 832 (2017).
- [34] J. M. Boss, K. S. Cujia, J. Zopes, and C. L. Degen, Quantum sensing with arbitrary frequency resolution, *Science* **356**, 837 (2017).
- [35] G. Wang, Y.-X. Liu, Y. Zhu, and P. Cappellaro, Nanoscale vector AC magnetometry with a single nitrogen-vacancy center in diamond, *Nano Lett.* **21**, 5143 (2021).
- [36] T. Joas, A. M. Waeber, G. Braunbeck, and F. Reinhard, Quantum sensing of weak radio-frequency signals by pulsed Mollow absorption spectroscopy, *Nat. Commun.* **8**, 964 (2017).
- [37] L. Thiel, Z. Wang, M. A. Tschudin, D. Rohner, I. Gutiérrez-Lezama, N. Ubrig, M. Gibertini, E. Giannini, A. F. Morpurgo, and P. Maletinsky, Probing magnetism in 2D materials at the nanoscale with single-spin microscopy, *Science* **364**, 973 (2019).

- [38] I. Gross, W. Akhtar, V. Garcia, L. J. Martínez, S. Chouaieb, K. Garcia, C. Carrétéro, A. Barthélémy, P. Appel, P. Maletinsky, J.-V. Kim, J. Y. Chauleau, N. Jaouen, M. Viret, M. Bibes, S. Fusil, and V. Jacques, Real-space imaging of non-collinear antiferromagnetic order with a single-spin magnetometer, *Nature* **549**, 252 (2017).
- [39] Y. Lu, T. Wei, F. Duerer, Y. Lu, N.-B. Ming, P. G. Schultz, and X.-D. Xiang, Nondestructive imaging of dielectric-constant profiles and ferroelectric domains with a scanning-tip microwave near-field microscope, *Science* **276**, 2004 (1997).
- [40] S. Asaad, V. Mourik, B. Joecker, M. A. I. Johnson, A. D. Baczewski, H. R. Firgau, M. T. Mądzik, V. Schmitt, J. J. Pla, F. E. Hudson, K. M. Itoh, J. C. McCallum, A. S. Dzurak, A. Laucht, and A. Morello, Coherent electrical control of a single high-spin nucleus in silicon, *Nature* **579**, 205 (2020).
- [41] P. V. Klimov, A. L. Falk, B. B. Buckley, and D. D. Awschalom, Electrically Driven Spin Resonance in Silicon Carbide Color Centers, *Phys. Rev. Lett.* **112**, 087601 (2014).
- [42] K. C. Nowack, F. H. L. Koppens, Y. V. Nazarov, and L. M. K. Vandersypen, Coherent control of a single electron spin with electric fields, *Science* **318**, 1430 (2007).
- [43] D. Bluvstein, Z. Zhang, and A. C. B. Jayich, Identifying and Mitigating Charge Instabilities in Shallow Diamond Nitrogen-Vacancy Centers, *Phys. Rev. Lett.* **122**, 076101 (2019).

Correction: The misspelling of the name of the seventh author has been fixed. The name of the 13th author was misspelled during the proof stage and has been set right.